ELSEVIER

Surface Science 472 (2001) 205–222

SURFACE SCIENCE

www.elsevier.nl/locate/susc

Kinetics and structure of O_2 chemisorption on Ni(1 1 1)

I.L. Bolotin, A. Kutana, B. Makarenko [1], J.W. Rabalais *

Department of Chemistry, University of Houston, Houston TX 77204-5641, USA

Received 9 January 2000; accepted for publication 23 October 2000

Abstract

The kinetics of O_2 chemisorption at low dose on Ni(1 1 1) and the nature of the chemisorption site have been studied at 300 and 500 K using time-of-flight scattering and recoiling spectrometry (TOF-SARS), low energy electron diffraction, and scattering and recoiling imaging code (SARIC) simulations. Variations in the TOF-SARS spectra with different crystal alignments during O_2 dosing provide direct information on the location of oxygen adatoms on the Ni(1 1 1) surface at very low coverages as well as site-specific occupation rates (S_{fcc} and S_{hcp}) and occupancies (θ_{fcc} and θ_{hcp}). A system of equations has been developed that relate the slopes of the scattering and recoiling intensities versus O_2 exposure dose to these probabilities and occupancies. The results identify three chemisorption stages as a function of oxygen exposure, each with its own specific occupation rates and occupancies. The *first-stage* is observed up to $\theta_1 = \theta_{fcc} \sim 0.21$ ML with $\theta_{hcp} = 0$, constant $S = S_{fcc} \sim 0.18 \pm 0.01$, and coverage ratio $w = \theta_{hcp}/\theta_{fcc} \sim 0$ for both 300 and 500 K. The *second-stage* is observed at coverages between $\theta_1 \sim 0.21$ and $\theta_2 \sim 0.32$ ML with constant $S_{fcc} = -(0.05 \pm 0.01)$ and $S_{hcp} = (0.16 \pm 0.02)$ at 300 K and $S_{fcc} = (0.005 \pm 0.003)$ and $S_{hcp} = (0.007 \pm 0.003)$ at 500 K, and coverage ratios $w = \theta_{hcp}/\theta_{fcc} \sim 1$ at 300 K and $w = \theta_{hcp}/\theta_{fcc} \sim 0.10$ at 500 K. The *third-stage*, observed for $\theta > 0.32$ ML, involves saturation coverage of the adsorption sites. SARIC simulations were used to interpret the spectra and the influence of oxygen chemisorption and vibrational effects. A method for determining the "effective Debye temperature Θ_D^*" that uses the experimental TOF-SARS intensity variations as a function of temperature and the simulated SARIC signals as a function of the mean square vibrational amplitude $\langle u^2 \rangle$ has been developed. The result for this system is $\Theta_D^* = 314 \pm 10$ K.

Keywords: Low energy ion scattering (LEIS); Computer simulations; Chemisorption; Nickel; Oxygen; Adsorption kinetics

1. Introduction

Oxygen chemisorption on nickel has provided a model system for dissociative chemisorption that has been subjected to a large number of surface science studies using many different techniques. The amount of data available for the Ni(1 1 1) surface is much less than that for the (1 0 0) and (1 1 0) surfaces, as summarized in Ref. [1] for the period prior to 1990. This is rather surprising since the close-packed (1 1 1) surface might be expected to be the simplest and, therefore, the first and most thoroughly studied. Investigations of the Ni(1 1 1)–O system in the last decade include studies of the phase diagram and critical phenomena in the

* Corresponding author. Tel.: +1-713-743-3282; fax: +1-713-743-2709.

E-mail address: rabalais@uh.edu (J.W. Rabalais).

[1] Permanent address: A.F. Ioffe Physical-Technical Institute, Russian Academy of Sciences, St. Petersburg 194021, Russian Federation.

0039-6028/01/$ - see front matter
PII: S0039-6028(00)00938-9

beginning stage of adsorption [2–6], the geometry of various phases [7–13], and thin oxide film formation [14–21]. Most of these works used low energy electron diffraction (LEED) [2–9,19,20], however X-ray photoelectron spectroscopy (XPS) [18,20], Auger electron spectroscopy (AES) [19], near edge X-ray absorption fine structure (NEXAFS) [12], electron energy loss spectroscopy (EELS) [13,15–18,20], adsorption calorimetry [14], and scanning tunneling microscopy [19,21] were also used.

The phase diagram for oxygen on Ni(1 1 1) has been studied in some detail [2,22,23] for the coverage range 0.1–0.34 ML (ML = monolayers; for Ni(1 1 1) 1 ML $\approx 1.9 \times 10^{15}$ atoms cm^{-2}) and temperatures of 150–500 K. At room temperature, exposure to O_2 gives rise to a $p(2 \times 2)$ LEED pattern. More precisely, at temperatures above 300 K a sharp $p(2 \times 2)$-O structure is observed only for coverage $\theta \sim 0.25$ ML. Based on LEED *I–V* measurements [2–9,21–24], Rutherford backscattering (RBS) [26,27], NEXAFS [13], and EELS [13] studies, it was concluded that the O adatoms in this $p(2 \times 2)$ structure occupy threefold hollow sites. The coverage scale was established by assuming that the maximum intensity $p(2 \times 2)$ pattern corresponded to $\theta = 0.25$ ML, i.e. a perfect $p(2 \times 2)$ lattice. Complications occur above $\theta =$ 0.25 ML. In the range $\theta = 0.25$–0.29 ML, splitting and streaking of the $p(2 \times 2)$ pattern is observed and interpreted [22,23] to be due to the formation of anti-phase $p(2 \times 2)$ domains. At coverages above ~ 0.28 ML, some authors report a $(\sqrt{3} \times \sqrt{3})R30°$ structure while others [1] do not. These different observations may arise from disordering transitions of the $(\sqrt{3} \times \sqrt{3})R30°$ structure near $\sim$300 K [2,22,23]. For coverages below 0.21 ML at 300 K and for all coverages at $T > 450$ K, oxygen exists as a lattice gas. At temperatures above 500 K oxygen dissolves into the bulk and is apparently independent of coverage [22,23]. This oxygen dissolution is not to be confused with oxide formation.

Due to the possibility of having a mixture of chemisorbed oxygen (conceivably in different phases), nickel oxide, and dissolved oxygen, structural determinations for this system are not straightforward. Structural determination for Ni(1 1 1)–O-$p(2 \times 2)$ has been mainly based on LEED *I–V* measurements [2,7,9,24,25] and RBS studies [26,27]. There are some variations in the models [7,9,24–27], although the common conclusion is that at room temperature and coverages less than 0.25 ML, chemisorbed oxygen atoms in fcc sites terminate the surface and the first-layer Ni atoms relax from their normal positions. In this long-range-ordered $p(2 \times 2)$ structure, only fcc sites are occupied [7,9] whereas at higher coverage it is possible to occupy hcp sites in a static disordered phase [4–6]. Recent LEED investigations [2,4–6] have shown that occupation of the hcp site can be thermally activated close to and above the order–disorder phase transition.

The kinetics and mechanism of oxygen chemisorption have been studied by AES and XPS as a function of O_2 exposure. AES measurements of oxygen uptake on Ni(1 1 1) [28–30] indicate that the occupation rate drops linearly with coverage from an initial value assumed to be 1.0 to an extrapolated saturation coverage near 0.33 ML. However, other studies [31] using AES report that the initial occupation rate is only $\sim$0.12 and that it actually increases with coverage to a value of $\sim$0.24 at $\sim$0.2 ML, before decreasing toward zero at a saturation coverage of 0.33 ML. Latter investigations using a single-crystal adsorption calorimeter [14] are still controversial.

In order to resolve these issues concerning the structure and kinetics of O_2 chemisorption on Ni(1 1 1), we have carried out a study of the system using time-of-flight scattering and recoiling spectrometry (TOF-SARS), scattering and recoiling imaging code (SARIC) simulations, and LEED as a function of O_2 dose in the temperature range 300–500 K. TOF-SARS probes the short-range order of a surface, i.e. <10 Å, and is therefore very sensitive to adsorbate site positions on a surface [32] at low adsorbate coverage. The new information obtained for this classical system is (1) direct observation and identification of the specific adsorption site, i.e. fcc or hcp, as a function of oxygen coverage, (2) site-specific occupation rates (S_{fcc} and S_{hcp}) and occupancies (θ_{fcc} and θ_{hcp}), identification of three adsorption stages as a function of O_2 exposure, each with its own specific occupation rates S_{fcc} and S_{hcp} and occupancies θ_{fcc}

and θ_{hcp}, and a method for determining the "effective Debye temperature Θ_D^*" from the data. A primary focus of the study is whether the chemisorption occurs via a direct channel or via an intermediate (chemisorbed or physisorbed) precursor state. In the former case, there should be a significant adsorption rate coverage dependence.

The paper is organized as follows. The following section describes the experimental technique and simulation method. Section 3 presents the experimental results from LEED and TOF-SARS measurements on the clean and O_2 exposed surfaces. Section 4 describes the SARIC simulations of the data and determination of the Debye temperature and site-specific occupation rates and occupancies. A comparison/discussion of the adsorption behavior in the three adsorption phases follows in Section 4. The results are summarized in Section 5.

2. Experimental methods and trajectory simulations

The measurements were carried out in a TOF-SARS spectrometer that has been described elsewhere [32]. Briefly, a rare gas pulsed ion beam impinging on a surface scatters and recoils atoms from the surface. The velocities of the keV ejected atoms are analyzed by measuring their flight times from the sample to a detector with fixed scattering angles θ of 60° (TOF drift region 1.6 m) and 90° (TOF drift region 1.5 m). The $\theta = 90°$ angle and a Ne^+ beam were used for acquisition of "blocking images" [33] for identification of the different $\langle 1\,1\,2\rangle$ azimuthal directions. All other measurements were made with $\theta = 60°$ and an Ar^+ beam. The pulsed beams were 3 keV, nominal pulse width ~80 ns, pulse rate of 30 kHz, average ion current of ~0.1 nA, beam divergence ~0.1°, and beam diameter of ~1 mm on the sample surface. The base pressure during the experiments was maintained below 3×10^{-10} Torr. The sample was mounted on a conventional manipulator that provides reproducible rotation in both azimuthal, δ, and incident, α, angles to ±0.5°. Good statistics are obtained with a non-destructive ion dose of $<10^{13}$ ions cm^{-2}. Since most of these scattered particles are neutral [34], the term "atoms" is used instead of "ions"; the detector has equal sensitivity to both of these when their energies are >1000 eV.

Ni single crystals in the form of disks 1 × 9 mm were polished within 0.5° of the [1 1 1] direction and cleaned by repeated cycles of 3 keV Ar^+ sputtering and annealing to 800°C. Annealing was accomplished by electron bombardment heating from behind the crystals. The surfaces were considered clean and well ordered when no impurity features were observed in the TOF-SARS spectra and the LEED images exhibited sharp (1×1) patterns. Oxygen dosing was done at a sample temperature of 300 and 500 K and O_2 pressures of $0.5–1 \times 10^{-8}$ Torr. The variation of the observed LEED pattern with oxygen coverage, as described in the literature [2,4–6,9,22,23], was used to determine the absolute value of the oxygen coverage on the surface. The $p(2 \times 2)$ structure was observed from a coverage of 0.21 ML up to 0.33 ML. We identify the coverage of >0.25 ML with a complex LEED pattern where the splitting and streaking of the $p(2 \times 2)$ pattern is observed. For the corresponding LEED patterns see Refs. [1,2,4–6,22,23].

Computer simulations based on the well-established classical theory of ion scattering [35] using the simulation program SARIC [36,37] were used to facilitate interpretation of the spectra. SARIC is based on the binary collision approximation, uses screened Coulomb potentials to describe the interactions between atoms, and follows the trajectories of all scattered and recoiled atoms in three-dimensions, thereby capturing both in- and out-of-plane single and multiple collision events. The primary ions impinge at random positions within the surface unit cell, simulating random impact parameter collisions. The Ziegler–Biersack–Littmark universal potential [38] was used for these specific simulations.

3. Experimental results

3.1. Low energy electron diffraction

The LEED patterns were monitored during O_2 exposure. Half-order spots corresponding to

the $p(2 \times 2)$ phase grew as a function of O_2 dose, rising to a maximum intensity and then decreasing again rapidly. Typical $p(2 \times 2)$ patterns were observed after an O_2 exposure of 1 L (1 Langmuir $= 10^{-6}$ Torr s which correspond to flux of $\sim 7.2 \times 10^{14}$ oxygen atoms cm^{-2}) and a sharp $p(2 \times 2)$ pattern was observed between 1.2 and 1.5 L. As described in previous works [2,4–9,22–29], this dose corresponds to a surface coverage of ~0.25 ML of oxygen with only a single type of site occupied for an ideal $p(2 \times 2)$ structure. With continued O_2 exposure at 300 K, the pattern became less sharp and clear. All the transformations of spots (splitting and streaking of the $p(2 \times 2)$ pattern) previously described [2,4–6,22,23] were observed. The $(\sqrt{3} \times \sqrt{3})R30°$ structure was not observed until an O_2 dose of 10–20 L (maximum in our investigations) and was observed only after remaining in vacuum over night. The reason for this may be that O_2 dosing was commenced immediately after annealing when the samples were still slightly above room temperature. Exposure of O_2 at 500 K resulted in only small background transformations and no superstructures were observed. This is in agreement with previous investigations [2,22,23] that have shown that above 450 K, oxygen exists only as a lattice gas. This condition allows us to compare TOF-SARS spectra from ordered and disordered oxygen adsorbate structures on Ni(1 1 1).

3.2. Time-of-flight scattering and recoiling spectrometry

3.2.1. Clean surface

Examples of typical experimental and simulated TOF-SARS spectra from a clean Ni(1 1 1) surface are shown in Fig. 1(a). Peaks due to scattered Ar and recoiled Ni are observed. These peaks are identified from the ion trajectories in the SARIC simulations as: Ar(S) – quasi-single scattering of Ar from Ni, Ar(DS) – quasi-double in-plane scattering, Ar(MS) – multiple out-of-plane "zig-zag" scattering, Ni(R) – quasi-directly recoiled Ni atoms from a quasi-single collision of impinging Ar, Ni(SR) – in-plane surface-recoiled Ni atoms resulting from sequences involving recoiling of Ni from impinging Ar followed by scattering of Ni from neighboring Ni atom(s), and Ni(MR) – out-of-plane surface-recoiled Ni atoms. There is good agreement between the experimental and simulated spectra. Similar spectral features have been discussed in detail elsewhere [34] and will not be repeated here.

The Ni(1 1 1) structure is shown in Fig. 2(a) and (b) as a plan view of the clean Ni(1 1 1) surface and a cross-section along the $[1\bar{2}1]$ azimuth illustrating geometrically different oxygen adsorbate sites. For identification of the geometrical positions of adsorbed oxygen atoms, it is necessary to identify the different $\langle 1\,1\,2 \rangle$ azimuths. All $\langle 1\,1\,2 \rangle$ directions are equivalent if only the topmost atomic layer with its sixfold symmetry is considered, while these directions are inequivalent if subsurface layers are considered. This difference is easily observed from ion scattering "blocking images" using a large-area detector as shown elsewhere [33]. In TOF-SARS, similar blocking effects with channeling [39] can be obtained by using light ions and a large scattering angle to enhance subsurface penetration and scattering; for this purpose, 3 keV Ne^+ and $\theta = 90°$ were used. This scattering angle is equal to the angular difference between the [1 0 1] and [0 1 0] directions (Fig. 2(b)). Direction $\langle 1\,1\,0 \rangle$ corresponds to the smallest interatomic distances in Ni and hence the largest blocking effects [33]. If the incident and exit angles are chosen as $\alpha \approx 35°$ and $\beta \approx 55°$, respectively, there are two possible alignments along the $[1\bar{2}1]$ azimuth (Fig. 2(b)): (1) incoming trajectories parallel to channeling direction [0 1 0] and outgoing trajectories parallel to blocking direction [1 0 1]; (2) incoming trajectories parallel to the $[2\bar{1}2]$ direction and outgoing trajectories parallel to the [1 4 1] direction. Note that the analyzing azimuths correspond to the direction from the ion gun to the detector in the plane of the $\langle 112 \rangle$ azimuths. In the first case, the alignment corresponds to the $[1\bar{2}1]$ "experimental" azimuth and in the second case, the alignment corresponds to the $[\bar{1}2\bar{1}]$ "experimental" azimuth, or the equivalent $[\bar{1}\bar{1}2]$ azimuth that is separated from $[1\bar{2}1]$ by 60°. Fig. 2(c) shows experimental data for these two different geometries. The solid and dashed lines correspond to two $\langle 1\,1\,2 \rangle$ azimuths that are separated by $\delta = 60°$. The dashed spectrum

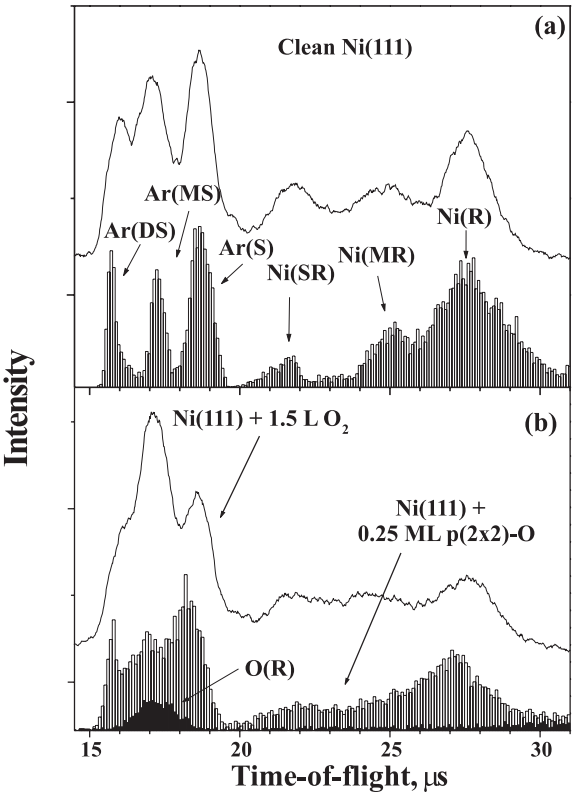

Fig. 1. Experimental (solid line) and simulated (vertical bars) time-of-flight spectra for 3 keV Ar^+ impinging on a (a) clean and (b) O_2 dosed Ni(1 1 1) surface. The peaks labeled Ar(S), Ar(DS), and Ar(MS) correspond to scattered Ar atoms ((S) – quasi-single, (DS) – quasi-double in-plane, (MS) – multiple out-of-plane), peaks labeled Ni(R), Ni(SR), and Ni(MR) correspond to recoiled Ni atoms ((R) – quasi-direct recoil, (SR) – surface-recoiled, (MR) – recoiled after multiple out-of-plane scattering), and the peak labeled O(R) corresponds to recoiled O atoms. The scattering conditions are: scattering angle $\theta = 60°$, beam incident angle from surface $\alpha = 30°$, and crystal azimuthal angle from $[1\bar{2}1]$ direction $\delta = 0°$. The vibrational amplitude used in the simulations was 0.06 Å.

exhibits low intensity due to only first-layer scattering while the solid spectrum exhibits high intensity due to scattering from both surface and subsurface layers. This indicates that the dashed spectrum corresponds to the first alignment discussed above, i.e. the incident angle α is parallel to the channeling direction [0 1 0] where scattering centers from subsurface atoms are shadowed and the exit angle β is parallel to the [1 0 1] direction where exit trajectories are severely blocked; this corresponds to the $[1\bar{2}1]$ azimuth. The solid spectrum corresponds to an incident angle ($[2\bar{1}2]$ azimuth) where subsurface scattering centers are visible and an exit angle ([1 1 4]) direction where there is less blocking of outgoing trajectories, i.e. as observed for the $[\bar{1}\bar{1}2]$ azimuth. SARIC simulations shown in Fig. 2(d) for these specific azimuthal alignments confirm this conclusion.

3.2.2. Oxygen chemisorbed surface

Examples of typical experimental and simulated TOF-SARS spectra from an O_2 dosed Ni(1 1 1) surface are shown in Fig. 1(b). The peak due to recoiled oxygen O(R) overlaps with the scattered Ar peaks. Two-dimensional plots of the intensity variations of the TOF-SARS signals in the recoiling region (21–31μs) and the scattering region (15.5–21 μs) as a function of flight time and incident angle α for the two azimuths $[\bar{1}\bar{1}2]$ and $[1\bar{2}1]$ are shown in Figs. 3 and 4, respectively. Plots for both the clean Ni(1 1 1) surface and the surface after adsorption of 1.2 L of O_2 at 300 K are shown.

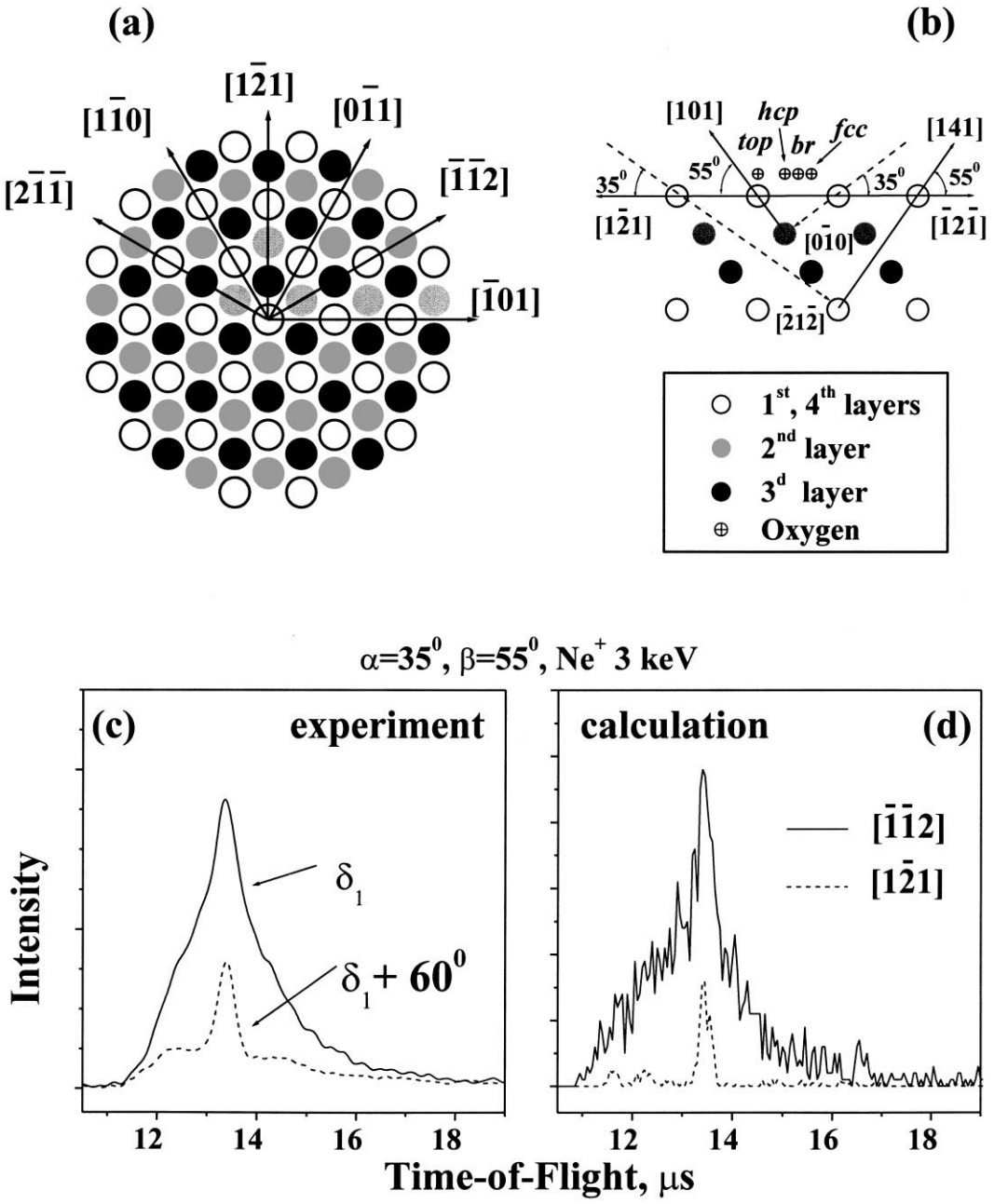

Fig. 2. (a) Plan view of the Ni(1 1 1) surface. (b) Cross-section perpendicular to the (1 1 1) surface along the [1$\bar{2}$1] direction. Four different oxygen adsorption sites (top, fcc, hcp, and bridge) are shown. (c) Experimental TOF-SARS spectra for the clean Ni(1 1 1) surface along two non-equivalent ⟨1 1 2⟩ azimuths that are 60° apart. (d) SARIC simulations of the TOF-SARS spectra for clean Ni(1 1 1) with identification of the two ⟨1 1 2⟩ azimuths used in the calculation.

An Ar^+ beam was used for scattering in order to enhance the first-layer sensitivity. The plots for both azimuths of the clean surface exhibit similar patterns in accord with the 60° periodicity of the

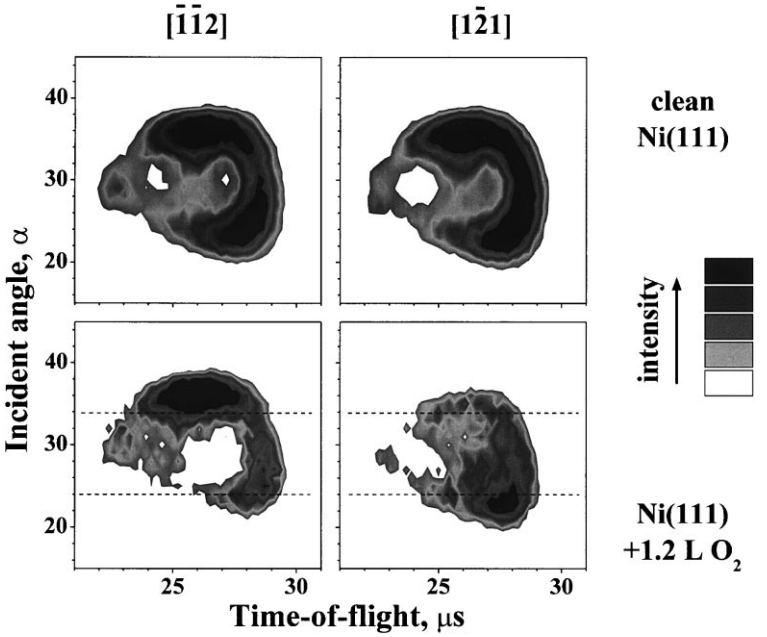

Fig. 3. Two-dimensional plots of the intensity variation of the TOF-SARS signals in the recoiling region (21–31 μs) as a function of flight time and incident angle, α, for two azimuths $[\bar{1}\,\bar{1}\,2]$ and $[1\,\bar{2}\,1]$. Top images – clean Ni(1 1 1). Bottom images – 1.2 L O_2 exposed surface at 300 K.

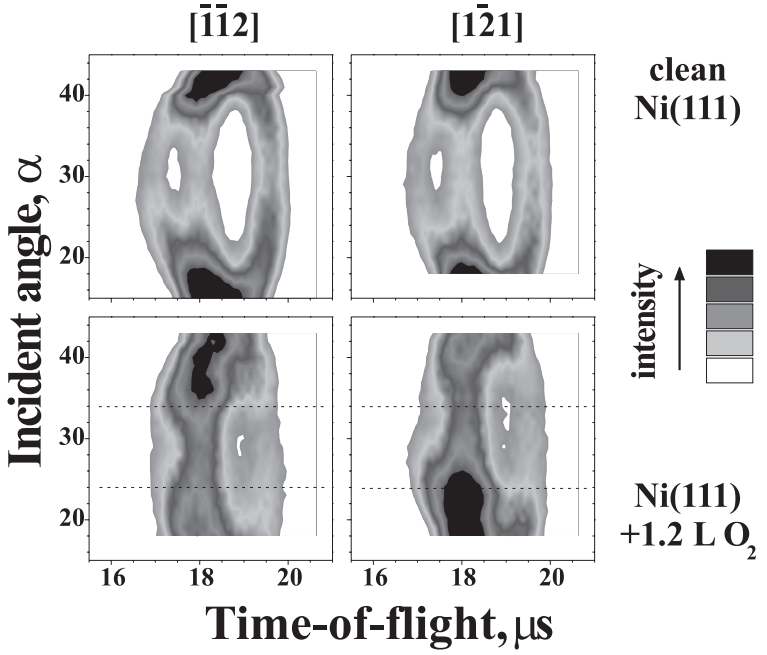

Fig. 4. Same as Fig. 3 for the TOF-SARS signals in scattering region (15.5–21 μs). For the O_2 dosed surface, this region also contains the oxygen recoil peaks.

first layer. This 60° periodicity no longer exists for the oxygen-covered surface. Instead, a 120° periodicity exists corresponding to adsorbate atoms occupying a single type of surface site. Note that the intensity variations for the oxygen covered surface in the scattering region (15.5–21 μs) contain mixed signals of both scattered Ar and recoiled O. The observed 120° periodicity for this region can only be explained by oxygen occupancy of a threefold hollow site. Occupancy of either the bridge or on-top sites (Fig. 2(b)) can be excluded since such occupancy would provide a 60° symmetry. The nature of the occupied threefold site, i.e. fcc or hcp, will be discussed in the following sections.

Dashed lines are drawn across the recoiling and scattering regions for the O_2 exposed surfaces of Figs. 3 and 4 at $\alpha = 24°$ and 34° where large differences in intensity are observed. Fig. 5 shows the TOF-SARS spectra corresponding to these two α values for the two azimuths identified above. For $\alpha = 24°$ there is a shift in the peak position of the recoil signal and for $\alpha = 34°$ there is a large intensity difference in the recoil signal. In the 15–20 μs region where both Ar scattering and O recoiling overlap, there is a large intensity difference for the two azimuthal directions, however spectra from both α values exhibit similar changes. The difference in recoil and scattering intensity at $\alpha = 34°$ will be used to monitor the kinetics of O_2 adsorption in the Section 3.3.

3.3. Kinetics of oxygen chemisorption

The uptake of oxygen on the surface was monitored by the intensities of the Ni recoil (R_{Ni}) signal in the region 21–31 μs and the Ni scattering plus O recoiling ($S_{Ni} + R_O$) signals in the region 15.5–21 μs. These intensities were normalized to the corresponding signals, i.e. R^0_{Ni} and S^0_{Ni}, from the clean surface for the $[1\bar{2}1]$ and $[\bar{1}\,\bar{1}\,2]$ azimuths. The results for adsorption of O_2 at both 300 and 500 K are shown in Figs. 6 and 7 versus exposure dose in Langmuirs. The three experiments (denoted by different symbols) indicate good reproducibility of the indicated dependencies. At 300 K the curves for R_{Ni}/R^0_{Ni} (Fig. 6) exhibit three stages. In the *first-stage*, a fast chemisorption phase for the $[1\bar{2}1]$ azimuth is observed up to ~1.2–1.3 L (or ~0.21–0.25 ML from the well developed, sharp $p(2 \times 2)$ LEED pattern at the end of the fast region). The largest difference in signals from the two different $\langle 1\,1\,2\rangle$ azimuths is observed at this point. In the *second-stage*, a fast chemisorption phase for the $[\bar{1}\,\bar{1}\,2]$ azimuth is observed up to ~2.2 L. At this point, similar intensities are obtained for both azimuths and the $p(2 \times 2)$ pattern persists

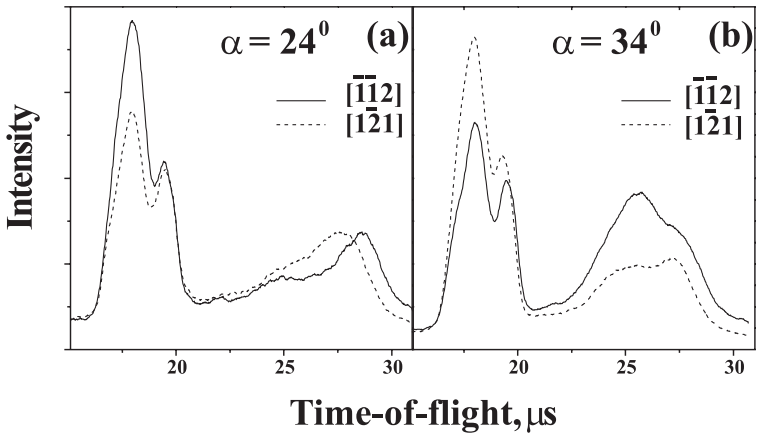

Fig. 5. TOF-SARS spectra along the $[1\bar{2}1]$ azimuth (- - -) and the $[\bar{1}\,\bar{1}\,2]$ azimuth (—) for two different incident angles 24° and 34° after adsorption of 1.2 L of O_2 at 300 K.

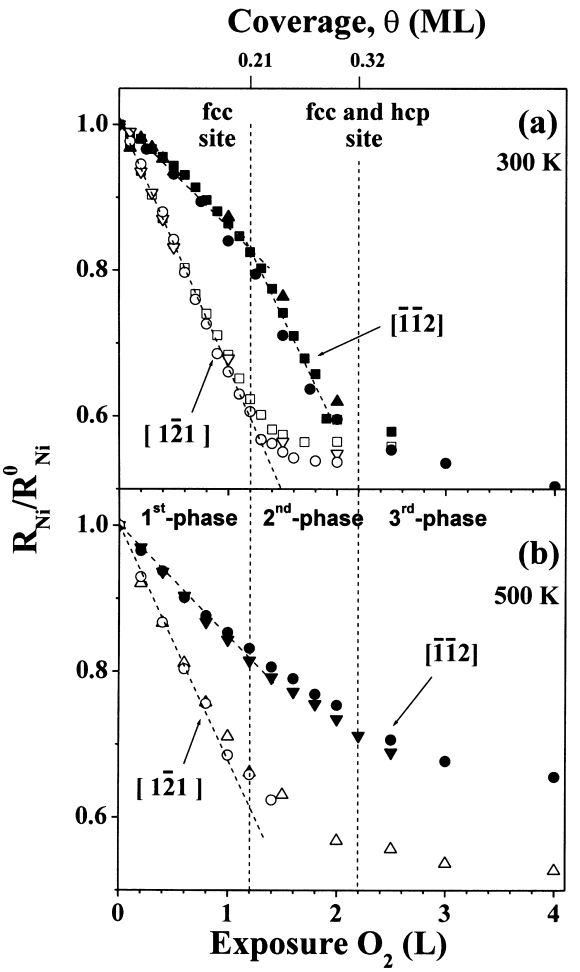

Fig. 6. Dependence of the normalized Ni recoil signal (R_{Ni}/R^0_{Ni}) on the O_2 exposure dose at (a) 300 K and (b) 500 K. The scattering conditions are: $\theta = 60°$, $\alpha = 34°$. The dashed lines represent the best linear fitting that delineates the adsorption regions. Solid symbols – $[1\bar{2}1]$ azimuth, open symbols – $[\bar{1}\,\bar{1}\,2]$ azimuth. The different types of symbols indicate three different experiments.

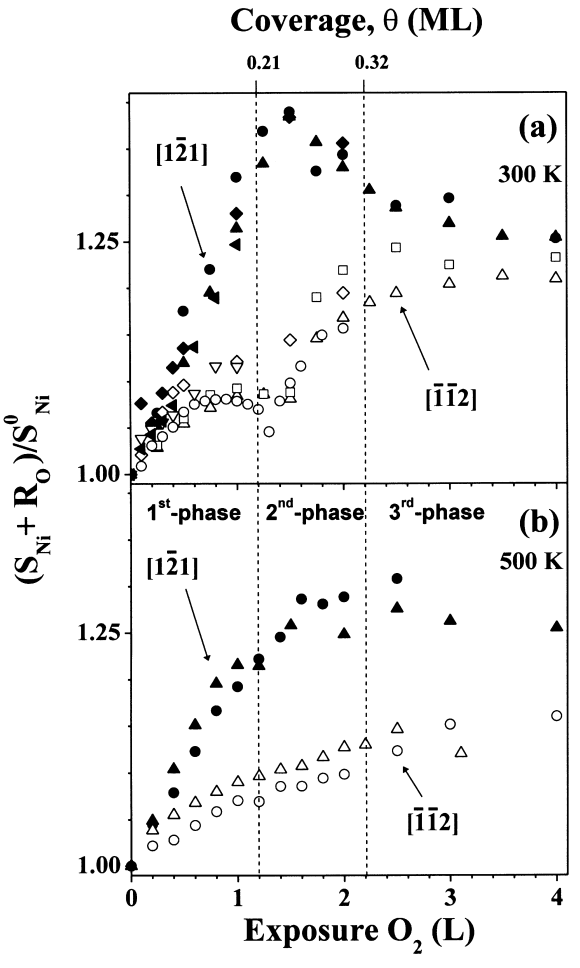

Fig. 7. Same as Fig. 6 for scattered Ar plus O recoil signals $(S_{Ni} + R_0)/S^0_{Ni}$.

with transformation of the LEED pattern (splitting and streaking of the p(2 × 2) spots) as described previously [2,4–6,22,23]. In *third-stage*, the intensities of both curves are similar and decrease slowly with dose. A three stage behavior is also observed for the $(S_{Ni} + R_0)/S^0_{Ni}$ curves in Fig. 7. Here there is a region between 1.0 and 1.4 L where a drop in intensity occurs for the $[\bar{1}\,\bar{1}\,2]$ azimuth. This phenomenon is related to the fact that when a well-ordered p(2 × 2) structure starts to form, the first Ni layer relaxes [41], resulting in a decrease in S_{Ni} for the $[\bar{1}\,\bar{1}\,2]$ azimuth. This will be confirmed by our SARIC simulations in Section 4.

These observations clearly show that at 300 K, initially only one preferred type of threefold hollow site is occupied up to ~0.21–0.25 ML, in agreement with [1–9,11,22–27]. As the coverage increases, the other three-fold site begins to fill along with formation of anti-phase domains of p(2 × 2) structure [2,4–6,22,23]. There are two processes occurring simultaneously, i.e. an increase in the occupancy of one type of threefold site and a decrease in the occupancy of the other threefold site, resulting in domains of p(2 × 2)

structure in the fcc sites adjoining domains of p(2 × 2)structure in the hcp sites. When the coverage reaches ~0.32 ML [2,4–6], there is equal occupation (~0.16 ML) of both threefold hollow sites and therefore no difference in the two investigated azimuths.

At 500 K, the behavior of both the R_{Ni}/R^0_{Ni} and $(S_{Ni} + R_0)/S^0_{Ni}$ signals are similar to those at 300 K up to ~1.2–1.5 L. At higher coverages, only a gradual decrease in R_{Ni}/R^0_{Ni} and gradual increase in $(S_{Ni} + R_0)/S^0_{Ni}$ with exposure is observed for both azimuths. This behavior is due to mixed occupancy of both the fcc and hcp sites [4–6].

At room temperature we did not observe any additional changes in the spectra as a function of time. However, after O_2 exposure at 500 K, the oxygen signal decreased almost linearly in time within a few hours. Following this, spectra similar to those of the clean surface before O_2 dosing were observed. This indicates that oxygen most likely desorbs at 500 K and does not dissolve into the bulk as it does at temperatures above 500 K [22,23]. Similar effects observed on Pd surfaces [40] have been attributed to oxygen depletion as a result of the diffusion of hydrogen atoms from the bulk to the surface where they react with the adsorbed oxygen, forming H_2O molecules that desorb readily at $T \geqslant 400$ K. We have not studied this phenomenon and will not focus on it in this paper.

4. Scattering and recoiling imaging code simulations

4.1. Structural model and vibrational amplitude

In order to conclusively determine whether the fcc or hcp site is preferred for the ideal p(2 × 2) structure (for 0.25 ML), the SARIC simulated spectra must be considered in more detail. Since we are depending on the observable intensities to be a reliable measure of the populations in each site, factors that can affect the scattering cross-sections should be considered. The first and most important parameter is the geometrical structure of the target surface. Three structural models from previous works [7,9,24–27] were used for simulating the Ni(1 1 1)–O system: (1) non-relaxed [24,25], (2) relaxed [9], and (3) relaxed with rotation of surface atoms [7]. The possibility for oxygen occupation of fcc or hcp. sites was checked for all models. In model (1), oxygen occupied a threefold hollow site at a distance above the surface of $d_\perp = 1.2$ Å [24,25]. In models (2) and (3), non-uniform relaxation of the first Ni layer was assumed with three-fourth of the Ni atoms relaxing outward and the remaining one-fourth unaffected (atoms not involved in bonding to oxygen) [7,9]. Model (2) used the relaxation proposed in [9], where the first-layer buckling is ~0.09 Å and oxygen occupies a threefold hollow site at a distance above the surface of $d_\perp = 1.11$ Å. Model (3) used the relaxation proposed in [7], where the first-layer buckling is ~0.12 Å, oxygen occupies a threefold hollow site at a distance above the surface of $d_\perp = 1.10$ Å, and the triplet of Ni atoms is rotated by ~2.2° (or lateral relaxation ~0.07 Å).

The second important parameter is temperature, i.e. for analysis of the ratio of scattering or recoiling intensities, the correct temperature dependent cross-section must be used. The choice of atomic thermal displacements for atomic collision simulations is a non-trivial problem. Most experiments based on keV ion bombardment are not particularly sensitive to thermal vibration effects. Errors in the treatments of vibrational effects will only significantly influence simulations of physical processes if the root mean square vibrational amplitude error is significant in comparison with the scattering cross-section. Most published keV bombardment simulations have not included thermal vibration effects.

In order to estimate the influence of vibrational effects on the spectra, Fig. 8 presents the Ni recoil intensity from experiments as a function of the sample temperature and from simulations as a function of the square of vibrational amplitudes $\langle u^2 \rangle$ for a clean Ni(1 1 1) surface. Both plots exhibit linear dependencies, providing a method for determining the "effective Debye temperature Θ^*_D" for our scattering measurements. Since $\langle u^2 \rangle \propto T$ (see Appendix A), the linear dependencies obtained from both plots yield $\Theta^*_D = 314 \pm 10$ K, or $u \sim 0.09$ Å at 300 K. The vibrational amplitudes of surface atoms are non-isotropic and can be separated into perpendicular and parallel compo-

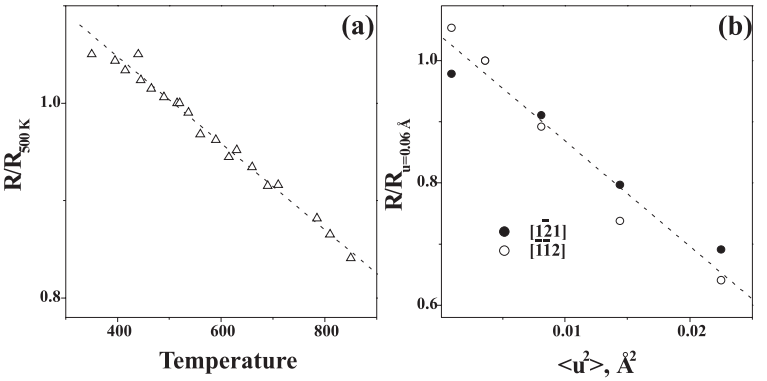

Fig. 8. Variation of the Ni recoil intensity as a function of (a) sample temperature in a TOF-SARS experiment and (b) vibrational amplitude u in SARIC simulations. The intensities were normalized to the value obtained at 500 K (experiment) and at $u = 0.06$ Å (calculation).

nents (or temperatures $\Theta_\perp$ and $\Theta_\parallel$). In order to compare the experimentally observed thermal vibrational amplitude (u from Θ_D^*) to the value estimated from $\Theta_\perp$ and $\Theta_\parallel$ ($u_\perp$ and $u_\parallel$, respectively), we use $\langle u^2\rangle(\Theta_D^*) \approx 2/3\langle u_\parallel^2\rangle + 1/3\langle u_\perp^2\rangle$. Table 1 shows the relationship between the isotropic mean square thermal vibration amplitude $\langle u^2\rangle$ and different values of Debye temperatures [4–6,41] at 0, 300, and 500 K. The values obtained for the vibrational amplitudes of Ni substrate atoms (with this Θ_D^*) are very close to the vibrational amplitudes for oxygen adsorbates on Ni(1 1 1) (see Table 1) if $\Theta_O^* = 580°$ K [4–6] is used. Details of the calculation of $\langle u^2\rangle$ are shown in Appendix A. The simulations were performed for $u = 0.03$, 0.06, 0.09, and 0.12 Å. The step value of ~0.03 Å is close to the difference in the vibrational amplitudes for 300 and 500 K. Each of these amplitudes was tested for the best correspondence to the experimental data.

Table 1
Relationship between the isotropic thermal vibration amplitude, $u = \sqrt{\langle u^2\rangle}$, and different values of the Debye and sample temperatures, T[a]

Debye temperatures	Thermal vibration amplitude, u (Å)		
	$T = 0$ K	$T = 300$ K	$T = 500$ K
$\Theta_B = 450$ K	0.03	0.06	0.08
$\Theta_\perp = 230$ K	0.05	0.12	0.15
$\Theta_\parallel = 389$ K	0.04	0.07	0.09
$\Theta_D^* = 314$ K	0.04	0.09	0.11
$\Theta_O^* = 580$ K	0.06	0.09	0.12

[a] Θ_B – bulk Debye temperature at 0 K, $\Theta_\perp$ and $\Theta_\parallel$ are the surface perpendicular and parallel Debye temperatures (all values from [42,43]). Θ_D^* – the "effective" Debye temperature described in the text. Θ_O^* – the "effective" Debye temperature for the oxygen adsorbate [4–6]. The calculations used Eqs. (A.4) and (A.5) from Appendix A.

4.2. Oxygen chemisorption

Tables 2 and 3 summarize the results of computer simulations for the three structural models and for four vibrational amplitudes. Only the results *for oxygen in the fcc site* are shown. Simulations with oxygen in the hcp site produced results that were the reverse of the experimental trends. The tables also include estimated values of normalized recoil intensities in the case of equal populations of hcp and fcc sites at a coverage of ~0.32 ML. These simulations provide an explanation for the experimentally observed (Fig. 7) drop in intensity in the scattering peak $(S_{Ni} + R_0)/S_{Ni}^0$ between 1.0 and 1.4 L. From Table 3 it is observed that this intensity is higher for the unrelaxed surface than for both of the relaxed surfaces. This is consistent with increased relaxation during formation of a well ordered $p(2 \times 2)$ structure as observed in [41]. Our simulation data for the ideal $p(2 \times 2)$ overlayer structure did not provide us with a direct way to select either of the

Table 2
Results of SARIC simulations of the normalized Ni recoil intensities for the three structural models using three different vibrational amplitudes[a]

Experimental intensity ratios $\frac{R_{Ni}}{R^0_{Ni}}[\bar{1}\,\bar{1}\,2]\Big/\frac{R_{Ni}}{R^0_{Ni}}[1\,\bar{2}\,1]$		u (Å)	θ^b (ML)	Model intensity ratio calculations $\frac{R_{Ni}}{R^0_{Ni}}[\bar{1}\,\bar{1}\,2]\Big/\frac{R_{Ni}}{R^0_{Ni}}[1\,\bar{2}\,1]$		
300 K	500 K			Model (1)	Model (2)	Model (3)
0.81|0.57 (1.2 L)	0.75|0.58 (1.5 L)	0.03	0.25	0.78|0.55	0.95|0.51	0.90|0.41
		0.06		0.72|0.61	0.76|0.57	0.74|0.45
		0.09		0.72|0.65	0.68|0.61	0.68|0.51
		0.12		0.76|0.77	0.69|0.65	0.69|0.58
0.57|0.56 (2.2 L)	0.65|0.52 (4 L)	0.03	~0.32	0.60[c]|0.60[c]	0.68[c]|0.68[c]	0.59[c]|0.59[c]
		0.06		0.60[c]|0.60[c]	0.60[c]|0.60[c]	0.52[c]|0.52[c]
		0.09		0.64[c]|0.64[c]	0.58[c]|0.58[c]	0.51[c]|0.51[c]
		0.12		0.72[c]|0.72[c]	0.60[c]|0.60[c]	0.56[c]|0.56[c]

[a] The values in the table are presented as the intensity ratios from two different 60° azimuthal directions, i.e. $R_{Ni[\bar{1}\,\bar{1}\,2]}/R_{Ni[1\,\bar{2}\,1]}$, and only for occupancy of the fcc sites at $\theta_1 = 0.25$. For occupancy of the hcp sites, the results are the inverse of the experimental results. Results for the three structural models discussed are presented in the table.

[b] The following coverage ratios were used for the model calculations. For $\theta_1 = 0.25$, hcp/fcc = 0 and for $\theta_2 = 0.32$, hcp/fcc = 1 at 300 K.

[c] Estimated values from 0.25 ML (see text).

Table 3
Same as Table 2 for normalized Ar scattering plus recoiled O intensities $(S_{Ni} + R_O)[\bar{1}\,\bar{1}\,2]/(S_{Ni} + R_O)[1\,\bar{2}\,1]$

Experimental intensity $\frac{S_{Ni}+R_O}{S^0_{Ni}}[\bar{1}\,\bar{1}\,2]\Big/\frac{S_{Ni}+R_O}{S^0_{Ni}}[1\,\bar{2}\,1]$		u (Å)	θ^a (ML)	Model intensity ratio calculations $\frac{S_{Ni}+R_O}{S^0_{Ni}}[\bar{1}\,\bar{1}\,2]\Big/\frac{S_{Ni}+R_O}{S^0_{Ni}}[1\,\bar{2}\,1]$		
300 K	500 K			Model (1)	Model (2)	Model (3)
1.06|1.40 (1.2 L)	1.10|1.29 (1.5 L)	0.03	0.25	1.03|1.76	0.91|1.57	0.85|1.23
		0.06		0.97|1.64	0.87|1.46	0.83|1.27
		0.09		0.93|1.44	0.87|1.35	0.83|1.24
		0.12		0.92|1.34	0.88|1.30	0.86|1.25
1.22|1.24 (2.5 L)	1.16|1.26 (4 L)	0.03	~0.32	1.47[b]|1.47[b]	1.29[b]|1.29[b]	1.05[b]|1.05[b]
		0.06		1.38[b]|1.38[b]	1.20[b]|1.20[b]	1.06[b]|1.06[b]
		0.09		1.22[b]|1.22[b]	1.13[b]|1.13[b]	1.05[b]|1.05[b]
		0.12		1.15[b]|1.15[b]	1.10[b]|1.10[b]	1.07[b]|1.07[b]

[a] The following coverage ratios were used for the model calculations. For $\theta_1 = 0.25$, hcp/fcc = 0 and for $\theta_2 = 0.32$, hcp/fcc = 1 at 300 K.

[b] Estimated values from 0.25 ML (see text).

three models used. Nevertheless, we included the simulation data for determination of the oxygen site, i.e. either hcp or fcc, and for complete consideration of the structural models proposed in the literature.

4.2.1. Site occupancies

Our model calculations assume a linear decrease in the relative recoil intensity (ΔR) during the *first* and *second-stages* as a function of the occupancies (in ML) of the fcc sites (θ_{fcc}) and hcp sites (θ_{hcp}). The linear portions of the recoil intensity plots of Fig. 6, that are also schematically represented in Fig. 9 at 300 and 500 K, were used to calculate the values of total coverage at the end of the second stage θ_2 and θ_{fcc}. This can be described as:

$$\begin{aligned} \Delta R_1 &= R^{(0)} - R^{(1)} = k_1\theta_1 = k_1\theta_{fcc}, \\ \Delta R_2 &= R^{(0)} - R^{(2)} = k_2\theta_1 = k_2\theta_{fcc}, \end{aligned} \tag{1}$$

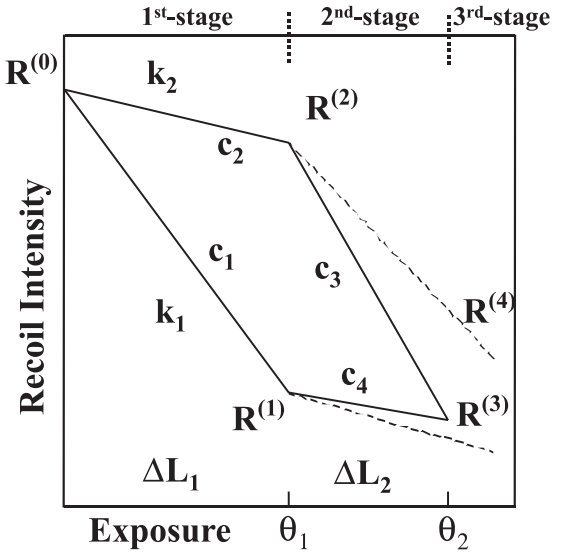

Fig. 9. Schematic diagram representing the variation of the Ni recoil intensities at 300 and 500 K that is used for calculations of occupation rate. The c_i's are the slopes of the linear portions of the recoil intensity plots. Points 1 and 2 correspond to termination of *the first-stage* of oxygen adsorption with coverage θ_1 (ΔL_1 total dose). Points 3 and 4 correspond to termination of the *second-stage* of oxygen adsorption with coverage θ_2 (ΔL_2 total dose).

where k_1 and k_2 are temperature and coverage independent azimuthal coefficients that describe the effect of adsorbed oxygen in specific sites on the scattering cross-sections, and $R^{(i)}$ are the values of the normalized recoil intensities at the stage boundaries (Fig. 9). For the *second-stage*, we write:

$$\begin{aligned}\Delta R_3 &= R^{(0)} - R^{(3)} = k_1\theta_{\mathrm{fcc}} + k_2\theta_{\mathrm{hcp}},\\ \Delta R_4 &= R^{(0)} - R^{(4)} = k_2\theta_{\mathrm{fcc}} + k_1\theta_{\mathrm{hcp}}.\end{aligned} \tag{2}$$

The four cases for which ΔR was calculated are shown in Fig. 9. Points 1 and 2 correspond to the termination of the *first-stage* of oxygen adsorption, characterized by occupation of only the fcc sites with a total coverage $\theta_1 = \theta_{\mathrm{fcc}} = 0.21$ (see below). Point 3, coinciding with point 4 at 300 K, corresponds to equal occupancy of both fcc and hcp sites, i.e. $\theta_{\mathrm{fcc}} = \theta_{\mathrm{hcp}} = \theta/2 \approx 0.16$ with total coverage $\theta_2 \sim 0.32$. Using Eqs. (1) and (2) at each point allows calculation of possible mixed occupancies between the two sites. This mixing can be quantified as $w = \theta_{\mathrm{hcp}}/\theta_{\mathrm{fcc}}$ and described as

$$\begin{aligned}&w = (\theta_2 - x\theta_{\mathrm{fcc}})/(\theta_2 + x\theta_{\mathrm{fcc}}),\\ &\quad \text{where } x = (\Delta R_3 - \Delta R_4)/(\Delta R_1 - \Delta R_2).\end{aligned} \tag{3}$$

From Eq. (3) it is straightforward to obtain w using ΔR_i for any dose between 0 and 4 L, providing a direct connection between O_2 dose and different site occupancies. For adsorption at 300 K and dose ~2.2 L, $x \sim 0$ and therefore $w \sim 1$, but for adsorption at 500 K, $x = 0.90 \pm 0.05$ and $w = 0.10 \pm 0.05$ for $\theta_2 \sim 0.25$ and $\theta_{\mathrm{fcc}} \sim 0.22$ (see below). These values of w are very close to values (~0.1–0.3) that we estimate from previous published results [12].

4.2.2. Occupation rates

From Eqs. (1) and (2), written for the experimental linear dependencies of the *second-stage* and using $k_{1,2} = c_{1,2}/S_1$, where c_i are the slopes of the linear portions of the recoil intensity plots, we obtain

$$\begin{aligned}c_3\Delta L_2 &= \frac{c_2}{S_1}\Delta\theta_{\mathrm{fcc}} + \frac{c_1}{S_1}\Delta\theta_{\mathrm{hcp}},\\ c_4\Delta L_2 &= \frac{c_1}{S_1}\Delta\theta_{\mathrm{fcc}} + \frac{c_2}{S_1}\Delta\theta_{\mathrm{hcp}},\end{aligned} \tag{4}$$

where $\Delta\theta_{\mathrm{fcc}} = \theta_{\mathrm{fcc}} - \theta_1$ and $\Delta\theta_{\mathrm{hcp}} = \theta_2 - \theta_{\mathrm{fcc}}$ are the changes in coverage in the *second-stage* for fcc and hcp sites, respectively, and $S_1 = \theta_1/\Delta L_1$ is the occupation rate (in ML per Langmuir) for the *first-stage*. Solving Eq. (4) for θ_{fcc} and θ_2, we obtain

$$\begin{aligned}\theta_2 &= \theta_1\left(1 + \frac{c_3 + c_4}{c_1 + c_2}\,\frac{\Delta L_2}{\Delta L_1}\right)\\ \theta_{\mathrm{fcc}} &= \theta_1\left(1 + \frac{c_1c_4 - c_2c_3}{c_1^2 - c_2^2}\,\frac{\Delta L_2}{\Delta L_1}\right).\end{aligned} \tag{5}$$

From these equations for 300 K, we find that $\theta_2 = \theta_1(1.50 \pm 0.05) = 0.32 \pm 0.01$ for $\theta_1 = 0.21$ and $\theta_{\mathrm{fcc}} = \theta_2/2 = 0.16 \pm 0.01$. For 500 K, $\theta_2 = \theta_1 \times (1.17 \pm 0.03) = 0.246 \pm 0.005$ and $\theta_{\mathrm{fcc}} = \theta_1(1.06 \pm 0.02) = 0.223 \pm 0.005$, giving $w = 0.10 \pm 0.05$. For these calculations, the termination of the *second-stage* was chosen at 2.2 L for 300 K (this is at the intersection of the experimental lines) and 4 L

for 500 K. The value of θ_2 at 300 K is very close to the well-known [1] 0.33 ML saturation coverage of the $(\sqrt{3} \times \sqrt{3})R30°$ ordered phase.

The coverage values obtained above can be used for calculating the total occupation rates S and partial occupation rates for fcc (S_{fcc}) and hcp (S_{hcp}) sites for the *first-* and *second-stages*. In our linear case, they are ratios of the change in total coverage, or coverage for a particular adsorption site, to the total dose in this stage. Since the *first-stage* corresponds to filling of the fcc sites, the occupation rates determined in this stage are $S = S_{fcc} = 0.18 \pm 0.01$ and $S_{hcp} = 0$ for both temperatures. For the *second-stage*, the total occupation rates are determined as $S \sim 0.11 \pm 0.02$ at 300 K and $S \sim 0.015 \pm 0.005$ at 500 K. The partial occupation rates are $S_{hcp} = 0.16 \pm 0.02$ and $S_{fcc} = -(0.05 \pm 0.01)$ at 300 K and $S_{hcp} = 0.007 \pm 0.003$ and $S_{fcc} = 0.005 \pm 0.003$ at 500 K. The negative value for S_{fcc} at 300 K depicts partial depletion of the fcc sites and/or migration of oxygen from fcc to hcp sites.

Summary results for the kinetics of oxygen adsorption at 300 and 500 K are presented schematically in Fig. 10. The thick, dark curves correspond to the dependencies of the total oxygen coverages (Fig. 10(a) and (c)), occupation rates (Fig. 10(b) and (d)) as a function of dose. The thin lines represent these same dependencies for the fcc and hcp fractional coverages. Here the solid lines correspond to the experimental observations and the dashed lines correspond to the approximations used above.

5. Discussion

Our results show that the combination of TOF-SARS experiments and SARIC simulations provides a sensitive probe of the chemisorption of O_2 on Ni(1 1 1). The combination can provide, within experimental error, a conclusive description of the oxygen adsorption site(s), site coverages θ, and occupation rates S along with the relaxed substrate geometry of the Ni(1 1 1)–O-p(2×2) system.

A system of equations has been developed that relate the slopes of the recoil intensities versus the O_2 exposure dose (L) to the specific occupancies (θ_{fcc} and θ_{hcp}) and occupation rates (S_{fcc} and S_{hcp}) of the fcc and hcp sites. The experimental results allow distinction of three chemisorption stages (Fig. 9). (1) The *first-stage*, observed up to a coverage of $\theta_1 = \theta_{fcc} \sim 0.21$–$0.25$ ML, is defined by a well-ordered p(2×2) LEED pattern and linear decreases of the recoil peak intensities with slopes c_1 and c_2 due to occupancy of only the fcc sites. This stage is the same for both temperatures. The O_2 dose span for this stage is 0–1.25 L (ΔL_1 total dose) and it terminates at the coverage $\theta_1 \approx 0.21$ ML where the slopes of the experimental lines begin to change for both 300 and 500 K. (2) The *second-stage*, observed at coverages between $\theta_1 \sim 0.21$ ML and $\theta_2 < 0.32$ ML, is defined by transformation of the LEED pattern at 300 K and linear decreases of the recoil peak intensities with slopes c_3 and c_4 due to occupancy of the hcp sites and partial depletion of the fcc sites. The O_2 dose span for this stage is 1.25–2.2 L (ΔL_2 total dose). At 300 K, the coverage ratio is $w = \theta_{hcp}/\theta_{fcc} \sim 0$ at $\theta_1 \sim 0.21$ ML due to occupation of only the fcc sites and increases to $w = \theta_{hcp}/\theta_{fcc} \sim 1$ at θ_2 (300 K) ~ 0.32 ML due to uniform occupancy of both types of three-fold sites. At 500 K, $w = \theta_{hcp}/\theta_{fcc} \sim 0.10 \pm 0.05$ at θ_2 (500 K) ~ 0.25 ML (at ~4 L) due to reduced occupancy of the hcp sites. (3) The *third-stage*, observed at O_2 doses greater than 0.33 ML at 300 K, is defined by a non-linear monotonic decrease in the recoil peak intensities with dose, indicating saturation of the adsorption sites.

Some earlier studies [1] of O_2 adsorption on Ni(1 1 1) at 300 K treated the kinetics by Langmuir expressions of the type $S = (1 - 4\theta)$ [28,29] and $(1 - 3\theta)$ [1]. These require coverage limits of 0.25 and 0.33 ML, respectively, with initial values $S_0 = 1$ that drop to zero final values. Our results indicate that the total occupation rates are constant and less than unity during the *first-stage* of adsorption up to a dose of 0.21 ML at both 300 and 500 K. These S values decrease by an order of magnitude on going to the *second-stage* of adsorption. Our results obtained at 300 K closely reproduce those of Stuckless et al. [14] and Winkler et al. [31] and are different from those reported by Holloway and Hudson [28,29] and Rieder [30]

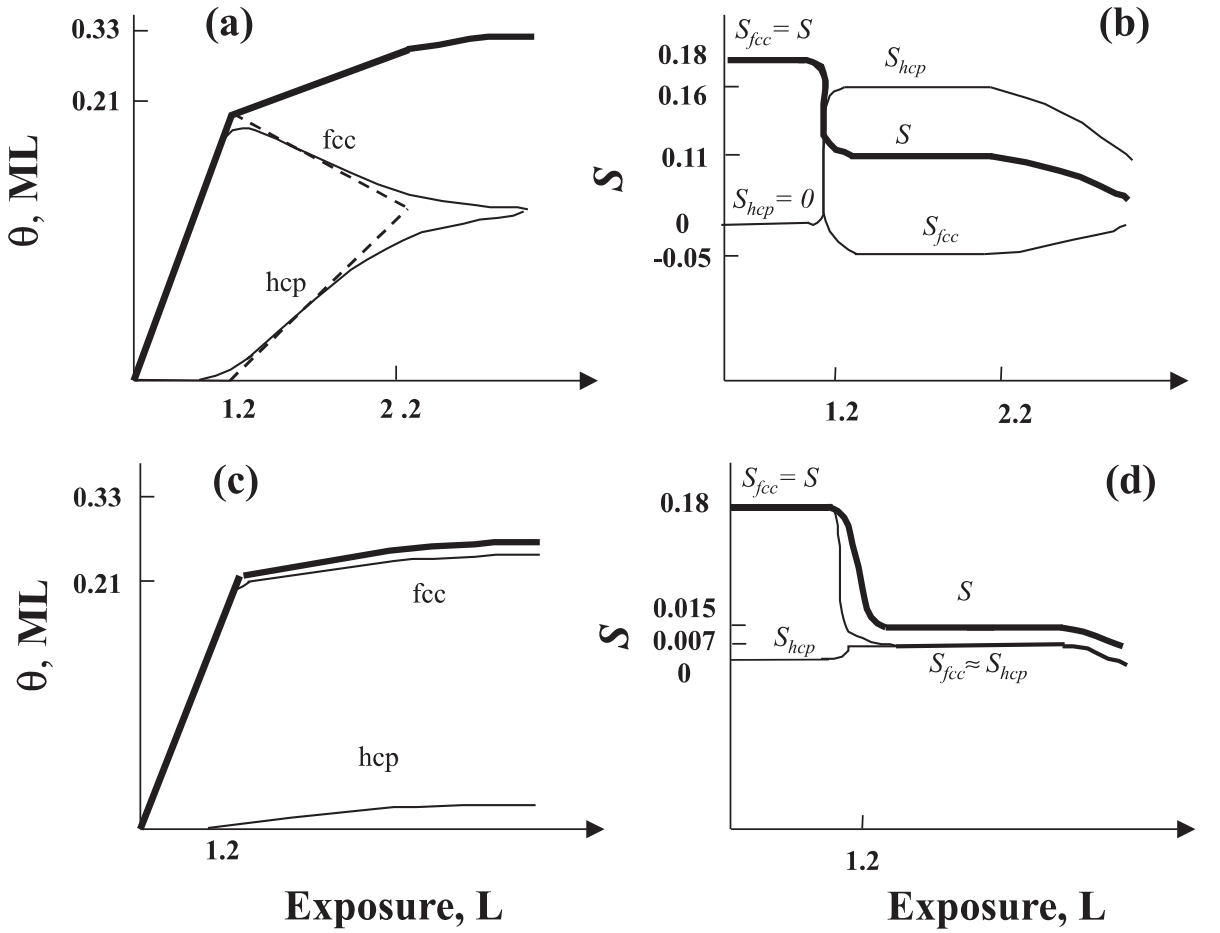

Fig. 10. Schematic phase diagrams representing the kinetics of O_2 chemisorption at (a,b) 300 K and (c,d) 500 K. The thick, dark curves correspond to the total oxygen coverage (θ) (a,c) and occupation rate (S) (b,d) as function of dose. The thin lines correspond to the θ's and S's of the fcc and hcp fractions. The solid lines are experimental curves and the dashed lines are from the calculations in this paper.

in a sense that the occupation rates change was very small in the initial stage of adsorption and there was an abrupt drop in S on going to the second stage. Stuckless et al. [14] report an initial occupation rates of $S_0 = 0.23$ that changes very slowly until ~0.25 ML, at which point S decreases but does not go to zero ($S \sim 0.02$ at 0.45 ML). Winkler et al. [34] obtained an initial value of $S_0 \sim 0.12$ that increased to ~0.24 at 0.25 ML and then decreased to a small value up to 0.33 ML. Both studies explained the occupation rates curves by precursor mediated adsorption kinetics, however they did not discuss the possibility of different adsorption sites and how this would affect occupation rates.

At 500 K we obtain the similar total occupation rate profile as at 300 K. Other studies [28,29,44] have also found similar values of occupation rates for this system at different temperatures. Therefore, the kinetics of oxygen adsorption at two different temperatures cannot be differentiated based on only the total occupation rate. The partitioning of the occupation rate S into partial components, i.e. S_{fcc} and S_{hcp}, provides us with insight into the adsorption and migration kinetics of the *first-* and *second-stages* of adsorption, since

we find that the hcp and fcc fractions during the *second-stage* of adsorption are different at 300 K and 500 K.

Theoretical treatment [45,46] of molecular adsorption on solids has established that occupation rates that are independent of surface adsorbate coverage are a result of the existence of an extrinsic precursor or trapping state [47–50], i.e. the O_2 molecule must dissociate before chemisorption. In our experiment, the occupation rate in the initial stage of adsorption showed very little or no dependence on the surface temperature and coverage, which is a sign of adsorption through an extrinsic precursor state [47]. Therefore, we assumed the adsorption to proceed through the precursor state. The same assumption for this system was made before, e.g. in a study of O/Ni(1 1 1) by a molecular beam technique [44]. The activation energy for this process is very small (or zero in our approximation) and cannot be measured given the error of our experiments and influence of surface vibrational amplitude on normalized recoiling or scattering intensity. The very close total and partial fcc occupation rate values obtained herein for 300 and 500 K in the *first-stage* is consistent with such a precursor state in which only the fcc sites are occupied in a non-ordered manner up to a dose of ~1.2 L, corresponding to a coverage of ~0.21 ML.

Analyzing the kinetics of the *second-stage* at 300 K, we obtain a negative occupation rate for fcc sites, $S_{fcc} = -(0.05 \pm 0.01)$. This is due to partial depletion of the fcc sites from migration of oxygen to hcp sites. Our results imply that at a coverage of 0.25 ML, there is already mixed fcc and hcp site occupation (the $\theta_{hcp}/\theta_{fcc}$ ratio is $w \sim 0.3$ from Section 4.2.1) and not an ideal fcc $p(2 \times 2)$ structure. The driving force for such a migration may be the formation of a $p(2 \times 2)$ long ordered structure with anti-phase fcc and hcp domains. The ordering energy may be greater than the energy difference between fcc and hcp sites and large enough to make the O atoms remain in the otherwise less energetically favorable hcp sites. This is at the cost of minimizing their total energy by ordering into a $p(2 \times 2)$ structure in hcp sites. This phenomenon is not observed at 500 K where both the fcc and hcp sites are filling simultaneously and the ordering is disturbed by the higher temperature.

6. Conclusions

We have shown that TOF-SARS is a sensitive probe of the adsorption sites of oxygen on a Ni(1 1 1) surface. The results identify three chemisorption stages: (1) *first-stage* – observed up to $\theta_1 = \theta_{fcc} \sim 0.21$ ML, well-ordered $p(2 \times 2)$ LEED pattern, linear decrease of the recoil peak intensity, and a constant occupation rate $S = S_{fcc} \sim 0.18 \pm 0.01$ and coverage ratio $w = \theta_{hcp}/\theta_{fcc} \sim 0$ for both 300 and 500 K. (2) *Second-stage* – observed at coverages between $\theta_1 \sim 0.21$ and $\theta_2 \sim 0.32$ ML, transformation of the LEED pattern, linear decrease of the recoil peak intensity, constant $S_{fcc} = -(0.05 \pm 0.01)$ and $S_{hcp} = (0.16 \pm 0.02)$ at 300 K and $S_{fcc} = (0.005 \pm 0.003)$ and $S_{hcp} = (0.007 \pm 0.003)$ at 500 K, and coverage ratios to $w = \theta_{hcp}/\theta_{fcc} \sim 1$ at 300 K and $w = \theta_{hcp}/\theta_{fcc} \sim 0.10$ at 500 K. The negative value of S_{fcc} at 300 K is due to to long range ordering effects. (3) The *third-stage*, observed at O_2 doses greater than 2.2 L, is defined by a non-linear monotonic decrease in the recoil peak intensities with dose, indicating saturation of the adsorption sites.

The SARIC simulations are able to reproduce the TOF-SARS spectra and provide interpretations for the experimentally observed effects of O_2 chemisorption on Ni(1 1 1). In addition, by using SARIC it is possible to decipher which parameters affect the scattering and recoiling intensities, such as the geometry of the adsorption site, surface relaxation, vibrational amplitudes, and adsorbate coverage. This is possible because both the single and multiple scattering contributions are included in the calculations as well as all of the symmetry elements of the surface structure. A method for determining the "effective Debye temperature Θ_D^*" that uses the intensity variations in the experimental Ni recoil signals as a function of temperature and the corresponding SARIC simulated signals as a function of the mean square vibrational amplitude $\langle u^2 \rangle$ has been developed. The results are $\Theta_D^* = 314 \pm 10$ K or $u \sim 0.09$ Å at 300 K.

Acknowledgements

This material is based on work supported by the National Science Foundation under Grant No. CHE-9986807.

Appendix A

According to the Debye theory, the isotropic mean square thermal vibrational amplitude, $\langle r^2\rangle$, of atoms in a monatomic solid is given by the following expression

$$\langle r^2\rangle = \frac{9(h/2\pi)^2 T}{Mk\Theta_D^2}\left[\phi(\Theta_D/T) + \frac{\Theta_D}{4T}\right], \quad (A.1)$$

where Θ_D is the Debye temperature, k is the Boltzmann constant, T is the absolute temperature, and M is the mass of atoms in the solid. $\phi(x)$ is the following function, where $x = \Theta_D/T$,

$$\phi(X) = \frac{1}{x}\int_0^x \frac{y\,dy}{e^y - 1}. \quad (A.2)$$

Eq. (A.1) refers to the mean square amplitude of an isotropic oscillator. For vibrations in a specific direction (x, y, or z), the right side of Eq. (A.2) must be divided by 3,

$$\langle u^2\rangle = \langle x^2\rangle = \langle y^2\rangle = \langle z^2\rangle = \langle r^2\rangle/3 = \frac{3\hbar^2 T}{Mk\Theta_D^2}\left[\phi(\Theta_D/T) + \frac{\Theta_D}{4T}\right]. \quad (A.3)$$

These unidirectional amplitudes are the quantities that are used in the SARIC simulations. Substituting for the physical constants, setting $x = \Theta_D/T$, and using M in atomic mass units, Eq. (A.3) simplifies to

$$\langle u^2\rangle = \frac{145.5}{M\Theta_D}\left[\frac{\phi(x)}{x} + \frac{1}{4}\right] \text{ Å}^2. \quad (A.4)$$

Using $\hbar = 1.05459 \times 10^{-34}$ J s, $k = 1.38066 \times 10^{-23}$ J K^{-1}, and 1 amu $= 1.6606 \times 10^{-27}$ kg, $\phi(x)$ can be calculated by numeric integration of Eq. (A.2). For values of x in the range 0–3.0 (or in the range $T = 0.33\ \Theta_D - \infty$), the following approximation is used [50]:

$$\phi(X) = \frac{1}{x}\int_0^x \frac{y\,dy}{e^y - 1} = 1 - \frac{x}{4} + \frac{x^2}{36} - \frac{x^4}{3600}. \quad (A.5)$$

If $T \to 0$, $\phi(x)/x \to 0$ and the lattice vibrations for Ni approach their zero-point levels ~0.03 Å.

References

[1] C.R. Brundle, J.Q. Broughton, in: D.A. King, D.P. Woodruff (Ed.), The Chemical Physics of Solid Surfaces and Heterogeneous Catalysis, vol. 3, Chemisorption Systems, Part A, Elsevier, Amsterdam, 1990, pp. 132–388.
[2] C. Schwennicke, H. Pfnür, Phys. Rev. B 56 (1997) 10558.
[3] Z. Li, X. Liang, M.L. Stutzman, J.A. Spizuoco, S. Chandavarkar, R.D. Deihl, Surf. Sci. 327 (1995) 121.
[4] C. Schwennicke, C. Voges, H. Pfnür, Surf. Sci. 349 (1996) 185.
[5] C. Schwennicke, H. Pfnür, Surf. Sci. 369 (1996) 248.
[6] L. Schwenger, C. Voges, M. Sokolowski, H. Pfnür, Surf. Sci. 307–309 (1994) 781.
[7] D.T. Vu Grimsby, Y.K. Wu, K.A.R. Mitchell, Surf. Sci. 232 (1990) 51.
[8] M.A. Mendez, W. Oed, A. Fricke, L. Hammer, K. Heinz, K. Müller, Surf. Sci. 253 (1991) 99.
[9] E. Schmidtke, C. Schwennicke, H. Pfnür, Surf. Sci. 312 (1994) 301.
[10] F. Mittendorfer, A. Eihler, J. Hafner, Surf. Sci. 433–435 (1999) 756.
[11] A. Eihler, F. Mittendorfer, J. Hafner, Phys. Rev. B 62 (2000) 4744.
[12] M. Pedio, L. Becker, B. Hillert, S. D'Addato, J. Haase, Phys. Rev. B 41 (1990) 7462.
[13] L.S. Caputi, S.L. Jiang, A. Amoddeo, R. Tucci, Phys. Rev. B 41 (1990) 8513.
[14] J.T. Stuckless, C.E. Wartnaby, N. Al-Sarraf, St.J.B. Dixon-Warren, M. Kovar, D.A. King, J. Chem. Phys. 106 (1997) 2012.
[15] J.A. Slezak, B.D. Zion, S.J. Sibener, Surf. Sci. 442 (1999) L983.
[16] Wei Li, M.J. Stiniman, S.J. Sibener, J. Vac. Sci. Technol. A 13 (1995) 1574.
[17] M.J. Stirniman, W. Li, S.J. Sibener, J. Chem. Phys. 103 (1995) 451.
[18] G.T. Tyiliev, K.L. Kostov, Phys. Rev. B 60 (1999) 2900.
[19] N. Kitakatsu, V. Maurice, P. Marcus, Surf. Sci. 411 (1998) 215.
[20] F. Rohr, K. Wirth, J. Libuda, D. Cappus, M. Bäumer, H.-J. Freund, Surf. Sci. 315 (1994) L977.
[21] S. Hildebrandth, Ch. Hagendorf, T. Doege, Ch. Jeckstiess, R. Kulla, H. Niddermeyer, Th. Uttich, J. Vac. Sci. Technol. A 18 (2000) 1010.
[22] A.R. Kortan, R.L. Park, Phys. Rev. B 23 (1981) 6340.
[23] L.D. Roelofs, A.R. Kortan, T.L. Einstein, R.L. Park, J. Vac. Sci. Technol. 18 (1981) 492.

[24] P.M. Marcus, J.E. Demuth, D.W. Jepsen, Surf. Sci. 53 (1975) 501.
[25] J.E. Demuth, D.W. Jepsen, P.M. Marcus, Phys. Rev. Lett. 31 (1973) 540.
[26] T. Narusawa, W.M. Gibson, E. Törnqvist, Phys. Rev. Lett. 47 (1981) 417.
[27] T. Narusawa, W.M. Gibson, E. Törnqvist, Surf. Sci. 114 (1982) 331.
[28] P.H. Holloway, J.B. Hudson, Surf. Sci. 43 (1974) 141.
[29] P.H. Holloway, J. Vac. Sci. Technol. 18 (1981) 653.
[30] K.H. Rieder, Appl. Surf. Sci. 2 (1978) 74.
[31] A. Winkler, K.D. Rendulic, K. Wendl, Appl. Surf. Sci. 14 (1982) 209.
[32] O. Grizzi, M. Shi, H. Bu, J.W. Rabalais, Rev. Sci. Instrum. 61 (1990) 740.
[33] I. Bolotin, L. Houssiau, J.W. Rabalais, J. Chem. Phys. 112 (2000) 7181.
[34] J.W. Rabalais, CRC Crit. Rev. Solid. State Mater. Sci. 14 (1988) 319.
[35] E.S. Parilis, L.M. Kishinevsky, N.Yu. Turaev, B.E. Baklitzky, F.F. Umarov, V.Kh. Verleger, I.S. Bitensky, in: Atomic Collisions on Solids, North-Holland, New York, 1993.
[36] S.S. Sung, V. Bykov, A. Al-Bayati, C. Kim, S.S. Todorov, J.W. Rabalais, Scan. Microsc. 9 (1995) 321.
[37] V. Bykov, C. Kim, M.M. Sung, K.J. Boyd, S.S. Todorov, J.W. Rabalais, Nucl. Instrum. Meth. Phys. Res. B 114 (1996) 371.
[38] J.F. Zeigler, J.P. Biersack, U. Littmark, in: J.F. Ziegler (Ed.), The Stopping and Range of Ions in Solids, Pergamon Press, NY, 1985.
[39] J.F. Van der Veen, Surf. Sci. Rep. 5 (1985) 199.
[40] H. Niehus, C. Achete, Surf. Sci. 369 (1996) 9.
[41] A. Grossmann, W. Erley, H. Ibach, Surf. Sci. 337 (1995) 183.
[42] D.P. Jackson, Surf. Sci. 43 (1974) 431.
[43] K. Mohammed, M.M. Shukla, F. Milstein, J.L. Merz, Phys. Rev. B 29 (1984) 3117.
[44] M. Beutl, K.D. Rendulic, G.R. Castro, Surf. Sci. 385 (1997) 97.
[45] P. Kisliuk, J. Phys. Chem. Solids 3 (1957) 78.
[46] P. Kisliuk, J. Phys. Chem. Solids 5 (1958) 78.
[47] M.A. Morris, M. Bowker, D.A. King, Simple processes at the gas–solid interfaces, in: C.H. Bamford, C.F.H. Tipper, R.G. Compton (Eds.), Comprehensive Chemical Kinetics vol. 19, Elsevier, Amsterdam, 1984, pp. 1–179.
[48] W.H. Weinberg, in: M. Grunze, H.J. Kreuzer (Eds.), Kinetics of Interface Reactions, Springer Series in Surface Sciences vol. 8, Springer, 1987, Berlin, p. 94.
[49] D.J. Auerba ch, C.T.Rettner, in: M. Grunze, H.J. Kreuzer (Eds.), Kinetics of Interface Reactions, Springer Series in Surface Sciences vol. 8, Springer, 1987, Berlin, p. 125.
[50] B.T.M. Willis, A.W. Pryor, Thermal Vibrations in Crystallography, Cambridge University Press, Cambridge, 1975, p. 125.